International Journal of Solids and Structures 49 (2012) 3148–3157

Contents lists available at SciVerse ScienceDirect

International Journal of Solids and Structures

journal homepage: www.elsevier.com/locate/ijsolstr

Microelastic wave field signatures and their implications for microstructure identification

M. Steven Greene [a], Stefano Gonella [b,*], Wing Kam Liu [c]

[a] Theoretical & Applied Mechanics, Northwestern University, Evanston IL, USA
[b] Department of Civil Engineering, University of Minnesota, Minneapolis MN, USA
[c] Department of Mechanical Engineering, Northwestern University, Evanston IL, USA

ARTICLE INFO

Article history:
Received 17 April 2012
Received in revised form 19 June 2012
Available online 29 June 2012

Keywords:
Elasticity
Microstructure
Dispersion
Damage
Wave propagation
Generalized continua

ABSTRACT

This work combines closed-form and computational analyses to elucidate the dynamic properties, termed signatures, of waves propagating through solids defined by the theory of elasticity with microstructure and the potential of such properties to identify microstructure evolution over a material's lifetime. First, the study presents analytical dispersion relations and frequency-dependent velocities of waves propagating in microelastic solids. A detailed parametric analysis of the results show that elastic solids with microstructure recover traditional gradient elasticity under certain conditions but demonstrate a higher degree of flexibility in adapting to observed wave forms across a wide frequency spectrum. In addition, a set of simulations demonstrates the ability of the model to quantify the presence of damage, just another type of microstructure, through fitting of the model parameters, especially the one associated with the characteristic length scale of the underlying microstructure, to an explicit geometric representation of voids in different damage states.

1. Introduction

This research aims to promulgate deeper understanding of unique wave propagation signatures and their ability to identify microstructural states in solids using computational microelasticity (Gonella et al., 2011) (ME) with a corresponding set of dynamic simulations. Thus, the focus of the study is on the parameters in the model and their effect on primarily the speed, but also the shape of propagating waves within a homogeneous, or undamaged, microelastic continuum. We reveal these signatures through detailed presentation of analytically derived dispersion relations (frequency-wavenumber $\omega(k)$) in one dimension (1D), which then serve as validation for numerical implementation. Dispersion is the situation when waves propagate with nonlinear dependence between their frequency ω and wavenumber k, thus producing non-constant phase and group velocities c_p and c_g as functions of frequency.

Undamaged, however, is somewhat of a misnomer since the growth of locally damaged regions in solids may be interpreted as the transition of one type of microstructure to another with a certain void size, property degradation, and morphology as shown in Fig. 1. This natural connection between damage and normal microstructure allows us to foresee implications of computational microelasticity for damage identification within the broad context of non-destructive evaluation (NDE).

As pointed out in a review of quantitative NDE methods (Achenbach, 2000), the progress of NDE depends on the measurement models with which to interpret input/output signals from the sensor network. Many such models employ equations of elastic wave propagation in solids (Achenbach, 1973) to estimate the condition of the structure of interest. The problem is a challenging one: reconstruct the state of the microstructure using only an input signal and any number of output signals at strategically placed sensors. While statistical learning methods (Yuan et al., 2005) are commonplace in modern NDE, the focus here is on the potential of computational ME (Gonella et al., 2011) to provide a more powerful physics-based analysis tool for signals tainted by some form of damage, and more broadly to explore the capability of ME to model microstructure states in heterogeneous solids.

The mathematical theory employed is that of elasticity with microstructure (Mindlin, 1964) wherein it is assumed material points are themselves continuum particles whose deformability is described by 9 additional degrees of freedom. Such theories are broadly referred to as *generalized* continuum theories, and detailed descriptions of these theories abound (Mindlin, 1964; Germain, 1973; Eringen, 1999; Vernerey et al., 2007). It is well know that equations of classical elasticity (CE) can not produce dispersive waves without direct numerical simulation (DNS) of

* Corresponding author. Tel.: +1 6126250866.
E-mail addresses: sgonella@umn.edu (S. Gonella), w-liu@northwestern.edu (W.K. Liu).

0020-7683/$ - see front matter © 2012 Elsevier Ltd. All rights reserved.
http://dx.doi.org/10.1016/j.ijsolstr.2012.06.011

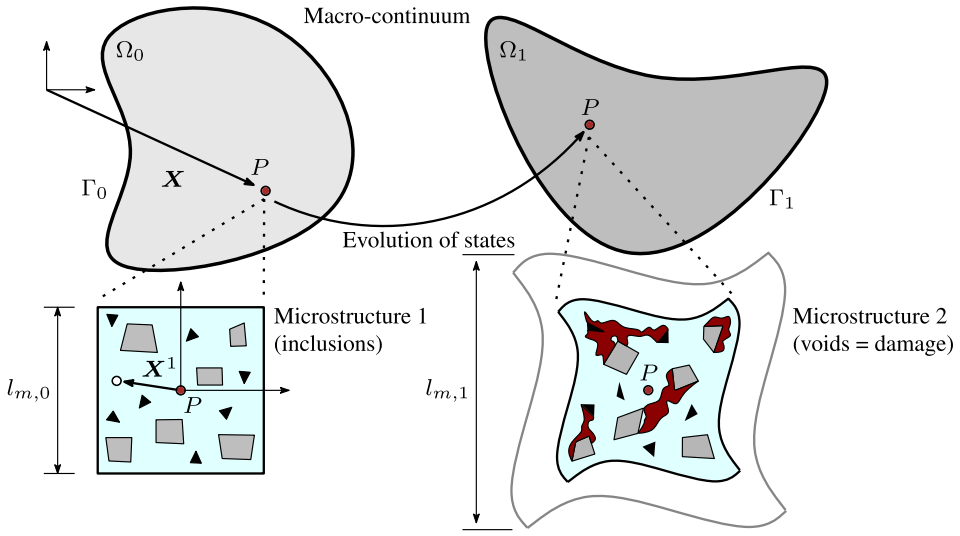

Fig. 1. Concept of microstructure transition as damage occurs. The figure on the left shows an initial state of the solid where the microstructure exists at some length scale but is intact. The right figure shows a hypothetical later damage state where voids have coalesced between microstructural features. Such voids have different properties and length scales than the initial microstructure, thus serving to change the characteristics of propagating elastic waves.

microstructure and/or defects, yet wave dispersion is experimentally observed in a multitude of materials, for instance fiber-reinforced composites (Tauchert and Guzelsu, 1972), concrete (Philippidis and Aggelis, 2005), human bone (Droin et al., 1998), and geomaterials like sand (Lai et al., 2002) and rock (Stavropoulou et al., 2003). Since CE does not capture this behavior, we use computational ME as a way to model the microstructure's effect on propagating elastic waves without its explicit geometric definition.

Studying wave propagation with theories of generalized continua is itself not new as Mindlin (1964) himself motivated his model with wave propagation and likened the wave dispersion it produces to that observed in neutron scattering experiments. The results presented herein point out far more detail of the model than the conceptual sketches previously presented. Other applications have been found with one commonality: as the structural features, either microstructure or macroscopic geometry, approache the wavelength of excitation, waves undergo a transition to dispersive behavior. On the geometric side, recent interest has focused on propagating waves in carbon nanotubes (Yoon et al., 2003; Wang, 2005; Askes and Aifantis, 2009; Song et al., 2010) with a suite of generalized continuum models used to capture the observed dispersive phenomena, though most of these are tailored to the nanotube application. High frequency geometry-induced dispersion in thin films has also been of interest (Ma and Maris, 2010). Of specific import to the present study are the theoretical developments in gradient elasticity (GE) derived from discrete lattice models and variational calculus (Metrikine and Askes, 2002; Askes and Metrikine, 2002; Metrikine and Askes, 2006; Gonella and Ruzzene, 2008; Polyzos and Fotiadis, 2012). The recent derivation of Polyzos and Fotiadis (2012) has exactly reproduced Mindlin's original model of gradient elasticity, which itself is a long wavelength reduction of the theory of elasticity with microstructure (Mindlin, 1964). Other studies have also focused on the numerical properties of GE within the context of both the finite element (Askes et al., 2007;Askes et al., 2008b) and boundary element (Polyzos et al., 2005; Vavva et al., 2009; Papacharalampopoulos et al., 2011) methods; the ability of GE to computationally produce wave dispersion is explicitly discussed by Bennett and Askes (2009). Of note is the work of Askes et al. (2008a); Papargyri-Beskou et al. (2009) who analytically explored the dispersive properties of waves propagating in gradient elastic continua; their results serve as both a motivator and benchmark of the analytical derivations contained herein.

Such studies demonstrate the promise felt by the solid mechanics community in utilizing high-order theories to explain dispersive wave propagation signatures that have consistently been observed experimentally in solids, though they also demonstrate that no consensus exists about which model is best. Recently, the authors of the present work studied the ability of ME in two spatial dimensions to produce positive pressure and shear wave dispersion whose presence becomes most pronounced when the wavelength of excitation of the solid overlaps the microstructural length parameter in the constitutive law (Gonella et al., 2011). This work improves the understanding of ME by adding to it the capability to capture negative dispersion, a phenomenon not broached in the past work but important for elastic wave propagation; we also corroborate previous arguments through the analysis process. By *positive* and *negative* dispersion, following the language of Erofeyev (2003), we mean a group wave velocity at finite frequencies that is greater and smaller, respectively, in magnitude than that in the low-frequency limit.

Unlike the models of GE (Metrikine and Askes, 2006), elasticity with microstructure posits an additional kinematic field to describe the deformability of microstructural unit cells which we expect to be of some use in characterizing microstructures and their anomalies or degradation over time. Further, the model is not restricted to rotational degrees of freedom (Suiker et al., 2001) describing the underlying microstructure, nor is it specific to an application of interest like nanowires (Song et al., 2010) where the additional degrees of freedom describe radial and angular strain in an idealized cylindrical structure. As described by Eringen (1999), the full geometric description of an elastic body's microstructure includes 3 independent directors for 9 total additional degrees of freedom that produce micro-longitudinal, micro-transverse, and micro-rotational wave propagation modes.

With such flexibility and generality, however, comes a greater degree of complexity in transient numerical implementation of the theory, definition of the additional material parameters in the constitutive law, and interpretation of the resulting wave fields, especially those of the additional kinematic variables. One attempt used physical phonon-dispersion relations of crystals to calibrate micromorphic constants (Chen and Lee, 2003), but this

method still did not provide physical meaning or general guidelines to the impact of micromorphic parameters on macroscopic behavior. Such challenges motivate our continued study of computational ME in an effort to both better understand the signatures of propagating waves in solids described by this model and to discuss implications such signatures have for microstructure identification in the context of NDE.

To do so, we adopt a two-step process. First, analytically derived dispersion relations for the 1D model and their sensitivity to ME parameters are studied in detail with focus given to mode shapes, wave velocities, asymptotic behavior of the same, and positive versus negative dispersion. The 1D ME equations are then implemented numerically and compared to CE DNS of two damage states, represented by deterioration of randomly populated element properties, at different frequencies. A numerical method for extraction of approximate phase and group velocities is also shown, and special attention here is given to the ultrasound frequency spectrum. The results show that ME surpasses GE in flexibility of capturing different propagation signatures and, we believe, offer great potential for the use of computational ME in non-destructive evaluation. This paper presents the ME equations, 1D analytical study, 1D numerical study with implications for identifying microstructural evolution, and conclusion in sequence.

2. Computational microelasticity: theory and numerics

For notational convenience, all italicized bold quantities indicate continuous field variables, for instance $\mathbf{v}(\mathbf{x},t)$, Einstein notation is used only where convenient with the standard sum on repeated indices, and the notation $\mathbf{v}_{,i} \equiv \partial \mathbf{v}/\partial x_i$. The equations governing a microelastic continuum are derived from the assumption that each point P in the macroscopic body is a particle containing internal deformability, recall Fig. 1. To model this internal deformability, an additional macroscopic 2nd order tensor field arises in the kinematic description of the solid from a linear Taylor series expansion of micro-displacements about the centroid of Ω^1, referred to hereafter as the *microstrain* $\boldsymbol{\varepsilon}^1$. As described by Germain (1973), such a description permits 3 contributions to the internal power of the solid from the standard macroscopic strain $\varepsilon_{ij} = (1/2)(u_{i,j} + u_{j,i})$, the relative deformation $\boldsymbol{\varepsilon} - \boldsymbol{\varepsilon}^1$, and the microstrain gradient $\boldsymbol{\varepsilon}^1 \overleftarrow{\nabla}$. These contributions all have energy conjugate stresses referred to as the macroscopic stress $\boldsymbol{\sigma}$, the relative stress $\boldsymbol{\tau}$, and the double stress $\boldsymbol{\mu}$.

From the statement of virtual work, summarized in (Gonella et al., 2011), we here take the 12 governing equations as (ignoring body forces):

$$(\boldsymbol{\sigma} + \boldsymbol{\tau}) \cdot \overleftarrow{\nabla} = \rho \ddot{\mathbf{u}} \text{ in } \Omega \tag{1a}$$

$$\boldsymbol{\mu} \cdot \overleftarrow{\nabla} + \boldsymbol{\tau} = \boldsymbol{\gamma}^1 \cdot \mathbf{I}^1 \text{ in } \Omega \tag{1b}$$

with the 12 boundary conditions

$$(\boldsymbol{\sigma} + \boldsymbol{\tau}) \cdot \mathbf{n} = \mathbf{t} \text{ on } \Gamma_t, \tag{1c}$$

$$\boldsymbol{\mu} \cdot \mathbf{n} = \mathbf{T} \text{ on } \Gamma_t, \tag{1d}$$

where the undefined quantities are the density ρ, second moment of micro-density $\mathbf{I}^1$, micro-acceleration $\boldsymbol{\gamma}^1$, surface normal $\mathbf{n}$, surface traction $\mathbf{t}$, surface couple $\mathbf{T}$, and domain definition Ω and Γ as shown in Fig. 1. For the remainder of the paper the micro-scale quantities contributing to the kinetic energy of the microelastic continuum will be defined following (Gonella et al., 2011; Vernerey et al., 2007):

$$\boldsymbol{\gamma}^1 = \ddot{\boldsymbol{\varepsilon}}^1, \quad \mathbf{I}^1 = \frac{1}{\Omega^1} \int_{\Omega^1} \alpha \rho \mathbf{y}^1 \otimes \mathbf{y}^1 \, dV^1 = \Lambda \alpha \rho \mathbf{1}, \tag{2}$$

where the micro-density $\rho^1 \equiv \alpha\rho$ and $\alpha \in [0,1]$ is a parameter relating the micro to macro density. Further, we assume the underlying micro-domain is a cube so that $\Lambda \equiv (1/12) l_m^2$, where l_m is the microscopic length parameter which, in Mindlin's theory, may be physically explained as the size of the underlying microstructural averaging domain as shown in Fig. 1, though the requisite size of this domain is in general unknown. $\mathbf{1}$ is the 2nd order identity tensor and $\otimes$ the dyadic product $v_i \otimes v_j = v_i v_j$.

Multiplying the strong form equations Eq. (1a) and Eq. (1b) by test function $\delta\mathbf{u}$ and $\delta\boldsymbol{\varepsilon}^1$, respectively, then integrating over the equation domains and applying the divergence theorem results in the weak form

$$\underbrace{\int_\Omega \left(\delta \mathbf{u} \overleftarrow{\nabla}\right) : (\boldsymbol{\sigma} + \boldsymbol{\tau}) \, dV}_{\delta W_{int}} + \underbrace{\int_\Omega \delta \mathbf{u} \cdot \rho \ddot{\mathbf{u}} \, dV}_{\delta W_{kin}} + \underbrace{\int_{\Gamma_t} \delta \mathbf{u} \cdot \mathbf{t} \, dS}_{\delta W_{ext}} = 0, \tag{3a}$$

$$\underbrace{\int_\Omega \left(\delta \boldsymbol{\varepsilon}^1 \overleftarrow{\nabla}\right) \vdots \boldsymbol{\mu} \, dV}_{\delta W_{int}} + \underbrace{\int_\Omega \delta \boldsymbol{\varepsilon}^1 : \left(\boldsymbol{\tau} + \boldsymbol{\gamma}^1 \cdot \mathbf{I}^1\right) dV}_{\delta W_{int}, \delta W_{kin}} - \underbrace{\int_{\Gamma_t} \delta \boldsymbol{\varepsilon}^1 : \mathbf{T}^1 \, dS}_{\delta W_{ext}} = 0 \tag{3b}$$

Here, δ means variation and W_{int}, W_{kin}, and W_{ext} are the internal, kinetic, and external energy whose sum must be zero by d'Alembert's principle of virtual power (Germain, 1973). The weak form is used for finite element discretization.

To complete the full model, the constitutive law for an isotropic material is generalized from (Gonella et al., 2011) as:

$$\begin{bmatrix} \boldsymbol{\sigma} \\ \boldsymbol{\tau} \\ \boldsymbol{\mu} \end{bmatrix} = \begin{bmatrix} \mathbf{C} & \gamma\mathbf{C} & \mathbf{0} \\ \gamma\mathbf{C} & \beta\mathbf{C} & \mathbf{0} \\ \mathbf{0} & \mathbf{0} & \Lambda\beta\mathbf{C} \otimes \mathbf{1} \end{bmatrix} \begin{bmatrix} \boldsymbol{\varepsilon} \\ \boldsymbol{\varepsilon} - \boldsymbol{\varepsilon}^1 \\ \boldsymbol{\varepsilon}^1 \overleftarrow{\nabla} \end{bmatrix}, \tag{4}$$

where $\mathbf{C} \equiv \bar{\lambda}\mathbf{1} \otimes \mathbf{1} + 2\bar{G}\mathbf{I}$ is the usual macroscopic linear elastic stiffness matrix for isotropic materials with Lamé parameters $\bar{\lambda}$ and $\bar{G}$; $\mathbf{I}$ is the 4th order identity tensor. The parameters β and γ define the stiffness due to the relative deformation at the macro and micro-scales and the coupling of the macroscopic and relative deformation, respectively. The lower-right entry of the constitutive matrix arises from the same averaging operation in the high-order inertia term of Eq. (2)

$$\mathbf{C}^{11} = \frac{1}{\Omega^1} \int_{\Omega^1} \beta \mathbf{C} \otimes \mathbf{y}^1 \otimes \mathbf{y}^1 \quad dV^1 = \Lambda\beta\mathbf{C} \otimes \mathbf{1}, \tag{5}$$

again assuming the underlying domain is a cube. We apply the restriction $\beta \in [0,1]$, and there is a natural positive definiteness condition on the microelastic tangent matrix $\partial\boldsymbol{\Sigma}/\partial\boldsymbol{\Lambda}$ in Eq. (4), where $\boldsymbol{\Sigma} \equiv [\boldsymbol{\sigma}, \boldsymbol{\tau}, \boldsymbol{\mu}]$ and $\boldsymbol{\Lambda} = [\boldsymbol{\varepsilon}, \boldsymbol{\varepsilon} - \boldsymbol{\varepsilon}^1, \boldsymbol{\varepsilon}^1 \nabla]$. This condition is given for the 1D case later and discussed in detail for the full model elsewhere (Mindlin, 1964).

To tailor ME to describe dynamic loading scenarios, we here relate the underlying length parameter l_m to the wavelength of excitation $\lambda = 2\pi/k$ by another parameter δ such that $l_m \equiv \lambda/\delta, \delta \in (0,\infty)$, which is a measure of how many microstructural averaging domains there are per wavelength. As shown previously (Gonella et al., 2011), when $\delta \gg 1$ the effect of the additional field $\boldsymbol{\varepsilon}^1$ is negligible on propagating waves; this situation's physical meaning is that the underlying microstructural features vary on far smaller a scale than the wavelength so that the input signal does not detect their presence.

We here take care to note the full dynamic implementation of computational ME, under the present assumptions, is described by 7 parameters: 3 at the macroscale $\{\rho, \bar{\lambda}, \bar{G}\}$, and 4 at the microscale $\{\alpha, \beta, \gamma, \delta\}$. This description is chosen so that we may later write analytical quantities pertinent to microelastic solids in ratios to terms familiar to classical continua. Plugging the constitutive law Eq. (4) into the governing equations Eqs. (1a), and (1b)

produces the following coupled linear PDE's, assuming minor symmetry on the constitutive matrix that accompanies isotropy:

$$(1+2\gamma+\beta)\mathsf{C}_{ijmn}u_{m,nj}-(\gamma+\beta)\mathsf{C}_{ijmn}\varepsilon^{1}_{mn,j}=\rho\,1_{ij}u_{j,tt} \tag{6a}$$

$$(\Lambda\beta)\mathsf{C}_{ijmn}1_{ab}\varepsilon^{1}_{ab,nj}+(\gamma+\beta)\mathsf{C}_{imjn}u_{n,j}-(\beta)\,\mathsf{C}_{imjn}\varepsilon^{1}_{jn}=(\Lambda\alpha)\,\rho\,1_{ij}\varepsilon^{1}_{mj,tt}, \tag{6b}$$

The immediate takeaway from this result is that CE is recovered if $\beta=\gamma=\alpha=0$ or if $\delta\to\infty$ ($l_m\to 0$) from the constitutive law in Eq. (4) and strong form Eq. (1). In addition, these equations draw several parallels with GE as studied in (Papargyri-Beskou et al., 2009; Askes and Metrikine, 2002). Namely, though GE does not have additional degrees of freedom, it does introduce a length scale through a parameter g attached to the higher order displacement derivative and separate length parameter h preceding the higher order inertia term. Here, $\Lambda\beta$ and $\Lambda\alpha$ are direct analogues of these quantities. However, the ME model also contains coupling terms involving both β and γ connecting the equations at the macroscale to those at the microscale. These terms, as will be shown, provide added flexibility in ME to capture low-frequency wave dispersion in heterogeneous solids.

The microelastic equations may be discretized for numerical solution through the weak form Eq. (3) with the standard Galerkin finite element method (Belytschko et al., 2000) using linear Lagrange interpolants. This method approximates a general vector function $v_i(\mathbf{x},t)=N_J(\mathbf{x})\mathsf{v}_{Ji}(t)$, where v_{Ji} are the nodal values in an element and N_J are the nodal shape functions, $J=1,2,\ldots,n_e$ with n_e nodes per element. Using the Galerkin projection the discretized finite element equations for the microelastic solid may be written as (Gonella et al., 2011):

$$\mathbf{M}\ddot{\mathbf{d}}+\mathbf{K}\mathbf{d}=\mathbf{f}_{\Gamma}, \tag{7}$$

where $\mathbf{M}$ and $\mathbf{K}$ are the generalized, global mass and stiffness matrices, $\mathbf{d}$ the degree of freedom vector (in general 12 per node), and $\mathbf{f}_{\Gamma}$ the external force vector. The steps taken between Eqs. (3) and (7) involve the standard discretization procedure and are given in detail in the authors' previous study (Gonella et al., 2011) as well as a study of static ME (Zervos, 2008) neglecting inertia. In the ensuing numerical calculations, time integration is performed with a Newmark-β scheme (Belytschko et al., 2000) with parameters $\beta_{NB}=1/4,\gamma_{NB}=1/2$, which is equivalent to an undamped trapezoidal rule. Although the scheme is unconditionally stable, we have ensured 30 elements per signal wavelength were used and the Courant number $cfl=(\Delta t/\Delta x)c<0.5$, with c the wave velocity. This fine space-time mesh was used to ensure negligible discretization errors, especially numerical dispersion that would conflict with our examination of model-induced dispersion.

3. Wave propagation signatures in microelastic solids

The complex model in Eq. (6) is degenerated to the 1D case and written it in matrix form as

$$\mathbf{K}_0\frac{\partial\mathbf{v}^2}{\partial^2 x}+\mathbf{K}_1\frac{\partial\mathbf{v}}{\partial x}+\mathbf{K}_2\mathbf{v}=\mathbf{M}\frac{\partial\mathbf{v}^2}{\partial^2 t}, \tag{8}$$

where $\mathbf{v}=[u_{11},\varepsilon^1_{11}]^{\mathrm{T}}$ is the solution vector and

$$\mathbf{K}_0=E\begin{bmatrix}1+2\gamma+\beta & 0\\ 0 & \Lambda\beta\end{bmatrix},\quad \mathbf{K}_1=E\begin{bmatrix}0 & -(\gamma+\beta)\\ (\gamma+\beta) & 0\end{bmatrix},\quad \mathbf{K}_2=E\begin{bmatrix}0 & 0\\ 0 & -\beta\end{bmatrix},\quad \mathbf{M}=\rho\begin{bmatrix}1 & 0\\ 0 & \Lambda\alpha\end{bmatrix}. \tag{9}$$

The sufficient and necessary condition for positive-definiteness of the microelastic tangent matrix in this system is

$$\gamma^2<\beta. \tag{10}$$

To find the dispersion relation for the hyperbolic system in Eq. (8), let the solution be a harmonic waveform given by

$$\mathbf{v}=\boldsymbol{\phi}e^{\imath(kx+\omega t)}, \tag{11}$$

where $\imath\equiv\sqrt{-1}$, k is the wavenumber, and ω is the angular frequency of the propagating wave. The goal is to find the dispersion relation $\omega(k)$ in terms of the model parameters. Plugging Eq. (11) into Eq. (8) produces the eigenvalue problem

$$\left[\left(k^2\mathbf{K}_0-\imath k\mathbf{K}_1-\mathbf{K}_2\right)-\omega^2\mathbf{M}\right]\boldsymbol{\phi}=0, \tag{12}$$

which is solved by setting the determinant of the matrix in brackets equal to zero upon plugging in the matrices given in Eq. (9). The problem for the two modes $\omega_{1,2}$ may be written as a quadratic equation for $\varpi\equiv\omega^2$ as in the standard $\varpi^2+b\varpi+c=0$ form, with the solution

$$\varpi_{1,2}=\omega^2_{1,2}=\frac{1}{2}\bar{c}^2\left[\left(r^2_\beta+r^2_\alpha\right)k^2+\frac{1}{\Lambda}r^2_\alpha\pm\sqrt{\left(r^2_\beta-r^2_\alpha\right)^2k^4+Dk^2+\left(\frac{1}{\Lambda}r^2_\alpha\right)^2}\right], \tag{13}$$

where $\bar{c}=\sqrt{E/\rho}$ is the macroscopic, homogenized wave velocity, r_α and r_β high wavenumber asymptotic wave velocity ratios, and D a function of the model parameters: 1.5

$$r_\alpha=\sqrt{\frac{\beta}{\alpha}} \tag{14a}$$

$$r_\beta=\sqrt{1+\beta+\gamma} \tag{14b}$$

$$D=\frac{2}{\Lambda}r^2_\alpha\left[r^2_\alpha(1+\alpha)+3\gamma\left(1+\frac{2\gamma}{3\beta}\right)\right]. \tag{14c}$$

The high wavenumber velocity asymptotes $k\to\infty$ of the acoustic mode are given as

$$\begin{cases}\alpha\geqslant\beta, & c(k\to\infty)=r_\alpha\bar{c}\\ \alpha<\beta, & c(k\to\infty)=r_\beta\bar{c}\end{cases}, \tag{15}$$

where c is the wave speed with no distinction between phase and group necessary because of the asymptotic wavenumber. This result proves for ME in the high wavenumber limit what was shown for GE (Papargyri-Beskou et al., 2009) (provided $\gamma>0$): positive dispersion exists when the length parameter attached to the higher order spatial derivative is larger than that attached to the higher order inertia. Since $r_\alpha<1$, the microelastic solid undergoes negative dispersion in the high wavenumber limit for $\alpha>\beta$. On the other hand, $r_\beta>1$ so that high wavenumbers correspond to positive dispersion when more weight is attributed to the high-gradient length parameter through β. Special attention is paid to the ratio α/β in the ensuing analysis of the model, which acts as a natural partition of the dynamic behavior of the microelastic solid and indicates a key signature of its physical characteristics, i.e. wave-guide behavior or wave-reflect behavior (Murakami and Hegemier, 1986) that correspond to positive and negative dispersion, respectively. At the long wavelength limit ($k\to 0$) for $\gamma=0$, the model's acoustic mode recovers CE with $\omega^2=(E/\rho)k^2$, verified in Fig. 2(a). As will be seen shortly $\gamma\neq 0$ produces different long wavelength behavior.

The acoustic and optical mode dispersion relations with $\gamma=0$ are plotted in Fig. 2 for a bar with macroscopic magnesium alloy material properties $E=49\,(\mathrm{GPa})$ and $\rho=1800\,(\mathrm{kg/m^3})$ so that $\bar{c}=5000\,(\mathrm{m/s})$. Based on these properties, constant normalization factors of $\omega_0=10\,(\mathrm{MHz})$ and $k_0=2000\,(/\mathrm{m})$ are used throughout the results section. In elasticity with microstructure, a second mode due to the added microstrain field exists with its own propagation signatures. The same type of optical modes exist in GE

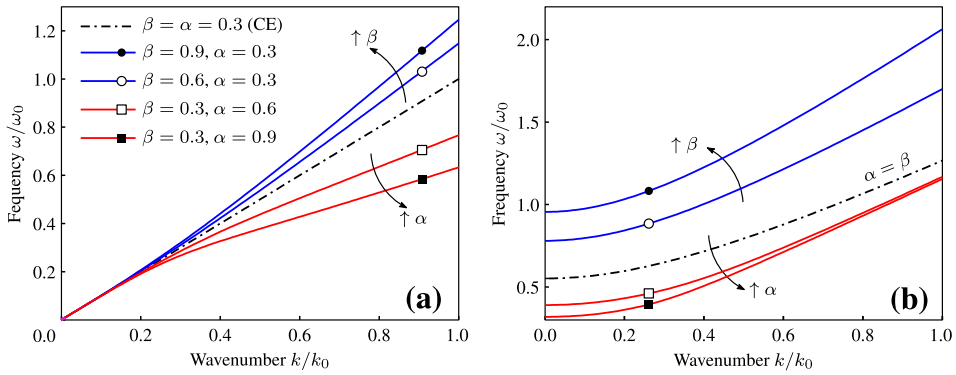

Fig. 2. Analytical quantities (a) displacement, the acoustic mode, and (b) microstrain, the optical model from solving 1D microelastic strong form with harmonic solution. Fixed quantities are $l_m = 2\pi/k_0$ and $\gamma = 0$.

models that contain 4th order time derivatives (see Askes et al., 2008a, Fig. 2 therein). Looking at the asymptotic behavior, as the wavenumber $k \to 0$, the acoustic mode frequency ω_1 converges to zero whereas the optical mode frequency ω_2 converges to a finite value given by

$$\omega_2(k=0) = r_\alpha \bar{c}\sqrt{\frac{1}{\Lambda}} = \sqrt{\frac{E^1}{I^1}}, \tag{16}$$

where $I^1 = \Lambda\alpha\rho$ comes from the low-right entry of the matrix **M** in Eq. (9) and $E^1 = \beta E$ has been defined as the central entry of the constitutive matrix in Eq. (4) in one dimension. This effect is shown clearly in the ω-intercept of Fig. 2(b) and and draws an interesting analogy with the classical elastic wave speed being the square root of *micro* stiffness over *micro* density divided by the length parameter introduced into the microelastic theory. The two modes shown in Fig. 2 compare well in both their shape and asymptotic behavior with those for GE "model 2" from Askes et al. (2008a). The markers in Fig. 2 are shown to indicate a curve that is the same between separate plots; these markers *do not* indicate data points, but the markers will carry to future plots to indicate the same parameter combinations.

Group velocities corresponding to the dispersion relation in Fig. 2(a) are plotted in Fig. 3(a) against frequency and against the ratio α/β in Fig. 3(b). The velocity values reported throughout this document are normalized by the CE solution $\bar{c} = 5000$ (m/s) to easily identify positive and negative dispersion. The group velocity is the tangent of the dispersion relation $c^g(k) = \partial\omega(k)/\partial k$ and physically represents the velocity of an entire traveling wave packet. The secant of the dispersion relation is known as the phase velocity which corresponds to the speed of a reference point in the signal.

Shown in this figure, and provable with algebra, is that when $\alpha = \beta$, which indicates the length parameters for the higher order inertia and stiffnesses are equivalent, and $\gamma = 0$, CE is recovered in the acoustic mode. This recovery is consistent with studies of GE (Mindlin, 1964; Papargyri-Beskou et al., 2009), though in general this is not true for ME if $\gamma \neq 0$ except in the high wavenumber limit $k \to \infty$. Fig. 3(b) shows that the degree of dispersion magnifies with frequency and $|1 - \alpha/\beta|$.

To expand comments on the model capability, Fig. 4 explores propagating wave signatures related to variation of the coupling parameter γ broken down into $\alpha/\beta < 1$ and $\alpha/\beta > 1$. In Fig. 4(a) the ratio $\alpha/\beta = 2$ so that the asymptotic high frequency velocities are fixed at $c(\omega \to \infty) = r_\alpha \bar{c}$. In Fig. 4(b), however, the high frequency velocity limits depend on γ as shown in Eq. (14b) since $\alpha/\beta < 1$. This high frequency γ independence and dependence of the group velocity is shown in Fig. 4(c) for the $10\omega_0$ curves which correspond to the high wavenumber limit. Furthermore, the coupling parameter is *the only* one to produce a positive-negative dispersion transition at finite frequencies. Increasing γ across all scenarios in Fig. 4 translates the low frequency $\omega \to 0$ velocities downward relative to the CE solution.

Such an observation warrants further examination as it appears the effect on propagating waves of γ is non-physical. The high sensitivity of the model at low frequencies to γ, however, may suggest its use in characterization of damage for structures since damage may work to soften a heterogeneous material by, as illustrated in Fig. 1, creating a soft voided network in the material. Such a decrease in apparent stiffness would work to effectively change the material, in a hyper-damaged state, creating lower wave velocities in the low frequency regime, an effect captured in ME by the coupling parameter γ but impossible to capture in GE which converges to CE unconditionally in the long wavelength limit.

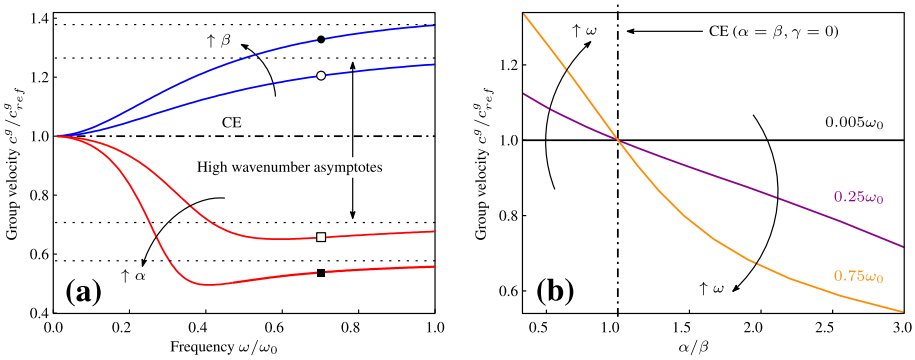

Fig. 3. Group velocity dependence on (a) frequency for iso-parameter α, β curves and (b) the ratio α/β for iso-frequency curves. Fixed quantities are $l_m = 2\pi/k_0$ and $\gamma = 0$.

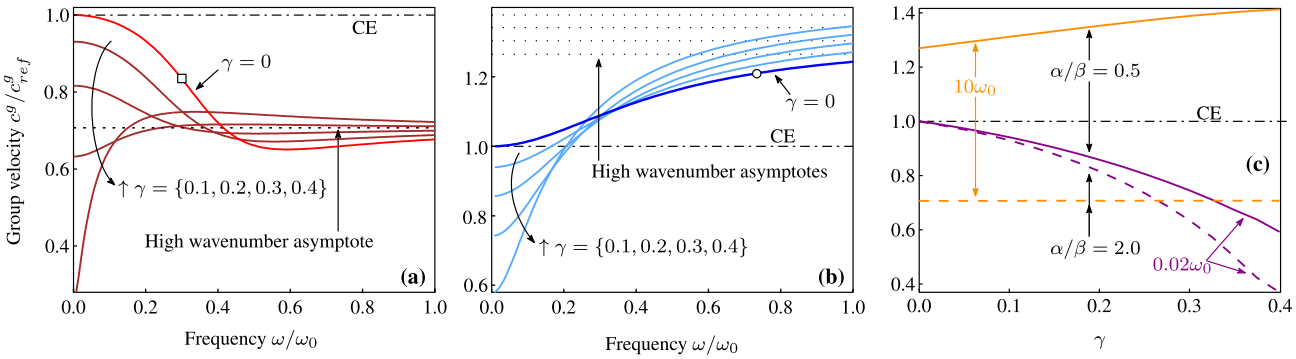

Fig. 4. Group velocity dependence on (a) frequency for iso-parameter γ curves with the ratio $\alpha/\beta = 2 > 1$, (b) frequency for iso-parameter γ curves with $\alpha/\beta = 0.5 < 1$, and (c) parameter γ for iso-frequency curves. Fixed quantities is $l_m = 2\pi/k_0$.

If the values of γ are taken as negative, an increasing translation of long wavelength wave speeds is observed of the same form as shown in Fig. 4 but mirrored about the classical solution. This observation warrants further comment. The equations solved here are Eq. (1), a set of coupled equations for the 1D harmonic problem in Eq. (9). However, recent derivations of *N*-scale micromorphic theory by (Vernerey et al., 2007) use a subtraction operation between $\boldsymbol{\sigma}$ and $\boldsymbol{\tau}$ in Eq. (1a) and between $\boldsymbol{\mu} \cdot \nabla$ and $\boldsymbol{\tau}$ in Eq. (1b), as well as a flipped sign in the relative kinematic measure in the constitutive law of Eq. (4). The end result is that to recover the elastic equations of Vernerey (Vernerey et al., 2007) using the equations herein, we require $\gamma < 0$, which would lead to the aforementioned positive translation of wave speeds to higher values at low frequency. It is not, therefore, necessarily non-physical that this material constant be negative. The only restriction on γ is that given in Eq. (10).

In addition to the dispersion induced by constitutive parameters β and γ, and inertia parameter α, the effect of the microscopic length parameter $l_m \equiv \lambda/\delta$ was also explored in Fig. 5 through a sweep of δ. Of note here is that for both cases $\alpha/\beta > 1$, $\alpha/\beta < 1$, decreasing the parameter δ, meaning the microstructural feature approaches and surpasses the wavelength in magnitude, exacerbates the observations of the previous discussions. This result is intuitive since l_m magnifies the absolute difference in length values attached to the high-order stiffness and inertia terms, $\Lambda|\alpha - \beta|$, in Eq. (6). In fact, as $\delta \to 0$, the velocities converge to their asymptotic values far faster, though this parameter does not translate the low frequency-limit wave propagation speed as does γ. This interesting feature allows for preservation of static equilibrium properties of solids while altering their dynamic character even at low frequencies. Of further interest is that the length parameter l_m is connected to the statistical characteristics of the underlying microstructure of the microelastic continuum, so that as microstructural features and structural anomalies evolve under deformation histories, these changes may be modeled with changes to l_m.

4. Numerical analysis and implications for microstructure identification

To discuss the model's implications for microstructure identification, we consider the bar shown in Fig. 6(a) for two scenarios: direct numerical simulation (DNS) of a damaged bar and an equivalent ME continuum. In subsection 4.1 we first describe the geometry, boundary condition, and mesh of the DNS simulation, second the quantities measured for comparison between DNS and ME, and third the code verification. Section 4.2 discusses the results of the computational ME simulations.

4.1. Problem setups and measured quantities

DNS is implemented by idealizing a damaged 1D domain as one with pseudo-randomly distributed imperfections in the bar material properties through the parameters $\psi, \nu_f \in [0, 1]$. ψ defines damage to the macroscopic material properties as $E_D = \psi E$, where E_D are the *damaged* properties and E the macroscopic axial modulus

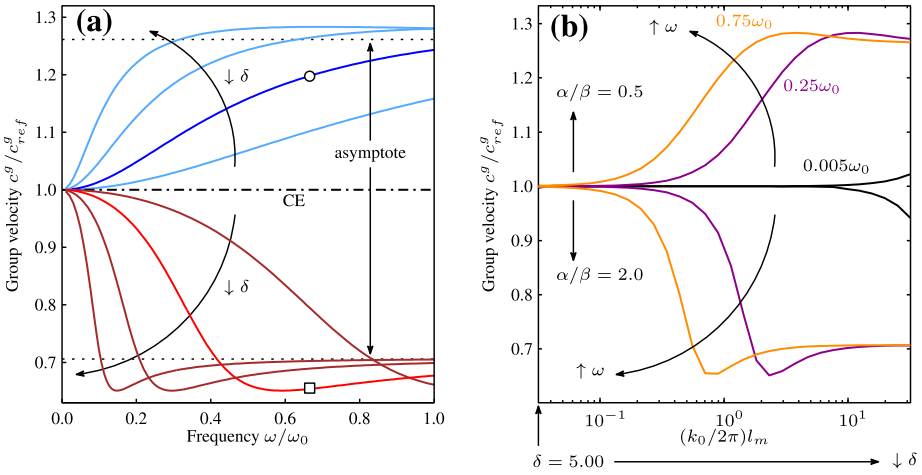

Fig. 5. Group velocity dependence on (a) frequency for iso-parameter $\delta = \{2, 1, 1/2, 1/4\}$ ($\lambda = 2\pi/k_0 = 2\pi\bar{c}/\omega_0$) curves, recall $l_m = \lambda/\delta$ with λ a reference wavelength, and (b) parameter δ for iso-frequency curves presented with normalized l_m values on the abscissa. Fixed quantities are $\alpha/\beta = 0.5, 2.0$ and $\gamma = 0$.

used in Section 3. v_f is the volume fraction of voids representing the damage state. The problem setup is shown in Fig. 6(a), with $L_{DNS} = 20\,(\text{cm})$ and the damaged region 4 (cm). As discussed in the introduction, the presence of damage may be thought of as a specific instance of general microstructural evolution processes. The goal of DNS is to measure the difference from the undamaged classical continuum, taken as the reference state, in transmitted signals through the 1D medium by both their shape change due to scattering phenomena and change in wave speed. These DNS simulations will be the benchmark by which to compare computational ME studies. In both, virtual sensors $s1$ and $s2$ with fixed spatial locations collect time history data of the propagating waveform which, by subsequent post processing, is compared among cases. The sensor locations are shown in Fig. 6(a).

The time-dependent loading signals are shown in Fig. 6(b). To analyze the frequency-dependent behavior of microelastic solids, we introduce a *chirp* signal $A(t)$ modulated by a Hann window given as a wide band signal containing frequency content described by

$$\omega_- \leqslant \omega \leqslant \omega_+, \tag{17}$$

where ω is the angular frequency of the exciting force applied to the domain. As $\omega_- \to \omega_+$, the signal converges to a Dirac-δ function in frequency space, though this is numerically unachievable. We approximate this condition with a narrow band *burst* given in the right of Fig. 6(b). The total time taken for one signal to pass is proportional to the inverse of the frequency content in the signal such that $t_B, t_C \sim 1/\omega$.

A trade-off between required spatial/temporal resolution and amount of frequency space which can be probed via one simulation exists between the chirp and burst signals. For wide band chirps, the coarseness of the space-time discretization is limited by the shortest wavelength to be resolved with the finite elements since waves at the tail end of the signal are traveling faster and have far shorter wavelengths than those at the front end. This means low-frequency content in the chirp is over resolved and computational resource wasted. At the same time, the more frequency content contained in the chirp excitation force allows a wider probe of frequency space, reducing the number of transient simulations to run to reconstruct dispersion curves numerically when compared to the burst signal.

For DNS the domain size two volume fractions of "voids" $v_f = \{10, 20\}\%$ were explored with voids having modulus reduction of $\phi = 0.5$. The DNS domain was set by numerical experiments to be large enough to capture the full transmitted signal in sensor $s2$ while avoiding boundary reflections. The size of the imperfections were taken as 2 finite elements for $v_f = 10\%$ at the center of the bar and each cluster increased to 4 elements for $v_f = 20\%$, see Fig. 6(a) for the illustration. A mesh of 4000 elements produced void sizes of 100 (μm) and 200 (μm) for the two damage states. For both damage states, the burst signal was used with amplitude magnitude $F_0 = 5\,(\text{kN})$ and DNS run for a total time of $T_{DNS} = 10t_B|_{\omega=0.1\omega_0}$. Signal quantities are shown in Fig. 6(b). The number of elements remained constant across all frequencies and corresponded to 35 elements per wavelength at the smallest wavelength.

For comparison between DNS and ME, two quantities are measured. The first is Δc_g, defined as the percent difference between the group velocity in the undamaged simulation with CE and either DNS or ME. The second quantity is ΔA, a measure of the percent change of the maximum signal amplitude as the wave travels from sensor $s1$ to sensor $s2$. ΔA attempts to measure distortion as the wave propagates through a damaged material. We take care to note that ΔA does not measure attenuation as all energy is conserved in microelasticity. In addition, the computational ME simulations do not capture the backscattering responsible for the wave amplitude reduction in the DNS simulations. While this is an inconsistency, we stress that the objective of this study is to capture global behavior – measured by Δc_g and ΔA – observed in microstructured solids without explicitly modeling the microstructure. Since group wave speeds are one quantity of interest, further mention must be made of the approach to numerically measure them. To extract estimated group velocities $\hat{c}_g$ in the space-time domain, we fix virtual sensor locations and record time histories. With the sensor locations x_{s1} and x_{s2} known and the centroid of the time history of the signal given by

$$\bar{t} = \frac{\sum_{j=1}^{N_T} t_j u(t_j)^2}{\sum_{j=1}^{N_T} u(t_j)^2}, \tag{18}$$

where there are N_T discrete points on the time history of the signal $u(t_j)$ and j is a time step index, the group velocity $\hat{c}_g$ is measured as

$$\hat{c}_g = \frac{\Delta x_s}{\Delta \bar{t}} = \frac{x_{s2} - x_{s1}}{\bar{t}_{s2} - \bar{t}_{s1}}, \tag{19}$$

where $\bar{t}_{s1}$ is the centroid of the time history at sensor $s1$.

The equivalent microelastic continuum, depicted in the bottom of Fig. 6(a), has the same macroscopic material properties E and ρ as the *undamaged* DNS elements and a smaller spatio-temporal domain with $L_{ME} = 10\,(\text{cm})$ and $T_{ME} = 4t_B|_{\omega=0.1\omega_0}$. The DNS domain is larger than the ME one to guarantee a representative damaged zone in the center of the bar with sensors placed at either side whose time histories are not polluted by boundary reflections. The authors recognize a more elegant solution would have been to implement non-reflecting boundary conditions, but such a step was not taken here as it would not impact the conclusions. Though the structure sizes are different, the spacing between sensors $s1$ and $s2$, where data collection occurs, are both 4 (cm) to allow for fair comparison between DNS and ME. Because of these considerations, the ME simulations are cheaper than DNS, a typical trend

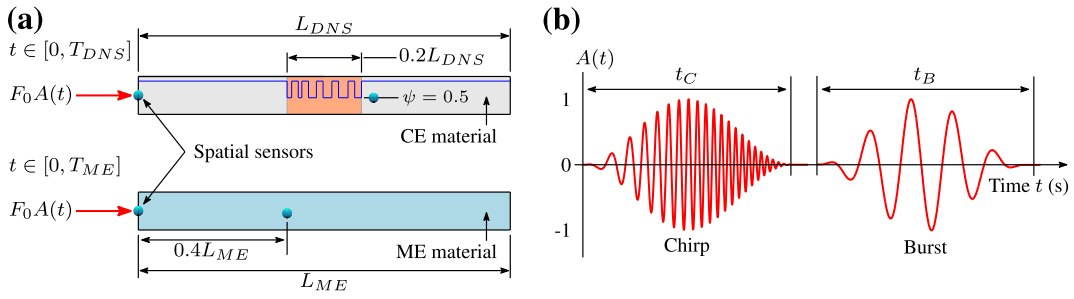

Fig. 6. 1D problem setup with (a) the simulation domains for direct numerical simulation of damage in the orange (shaded) zone of the top bar and equivalent microelastic continuum in the bottom bar. In (a), domains sizes $[L \times T]_{CE}$ and $[L \times T]_{ME}$ are different sizes. (b) Shows the traction boundary condition amplitude time histories.

in theories of generalized continua only magnified in higher dimensional space.

The ME bar is discretized by varying numbers of elements that depend on the frequency of the burst signal applied, with each simulation having 40 microelastic elements per wavelength. Fig. 7 shows both space-time and wavenumber-frequency domain methods for analysis of numerical wave fields and is used to verify the implementation of computational ME. Space-time data is transformed to Fourier space with the discrete Fourier transform (DFT) approach, and the numerical field data for the acoustic mode in Fig. 7(b) is shown to be accurate by its fit to the analytical solution with the same parameter combination. The parameter choice is $\{\alpha, \beta, \gamma, \delta\} = \{0.3, 0.9, 0.0, 10\}$. This verification was achieved using the chirp signal in Eq. (17) with $\omega_- = \omega_0/10$ and $\omega_+ = 8\omega_-$. The positive dispersion observed in Fig. 7(b) is consistent with the derivations in Section 3 for $\beta > \alpha$, cf. Fig. 2(a).

4.2. Simulation results and discussion

With a simple trial and error procedure, the length parameter l_m was calibrated to approximately fit the DNS group velocity results, with other ME parameters fixed at $\alpha = 0.5$, $\beta = 0.2$, and $\gamma = 0$. Emphasis for calibration on the length parameter l_m was chosen because it has a distinct physical meaning being a length scale related to microstructure of a material. The other parameters have found loose physical meaning in GE derivations from discrete lattice models (e.g. Askes and Metrikine, 2002), but always in a phenomenological sense. The manual calibration process only minimizes error between DNS and ME by inspection. An automated calibration is not necessary because we only aim to show that ME captures the observed trends. This calibration led to $l_m = 455\,(\mu\text{m})$ for the first damage state ($v_f = 10\%$) and $l_m = 769\,(\mu\text{m})$ for the second ($v_f = 20\%$). Since the length parameter was taken as constant across all frequencies, the parameter δ changed since it is a relation between the microzone length parameter and the applied signal wavelength $\delta = \lambda/l_m$. For damage state 1 $\delta = \{11, 6.5, 3.\bar{6}\}$ and for damage state 2 $\delta = \{6.5, 3.25, 2.1\bar{6}\}$. The increase of group velocity reduction observed here as δ decreases is the same trend observed for positive dispersion by Gonella et al. (2011) as the signal wavelength overlaps the microelastic length parameter.

The CE centroid $\bar{t}_{CE}$ and the time histories of the receiving sensor $s2$ for the three simulation frequencies are shown in Fig. 8 for the first damage scenario $v_f = 10\%, \psi = 0.5, l_m = 455\,(\mu\text{m})$. In this figure, the CE centroid arrives at $s2$ before the centroid of the DNS/ME waves, indicating an expected reduction in the measured group velocity upon the introduction of damage. The second quantity ΔA, the reduction in peak amplitude of the signal, may also be seen in Fig. 8. From the figure, both ME quantities approximately match the DNS simulation.

Quantitative analysis of the two metrics is catalogued in Table 1. There, we see quantitatively what may be deduced qualitatively from Fig. 8: that ME approximately captures the reduction in group velocity and the peak signal amplitude relative to the undamaged solid. This is exemplified by the closeness of the Δc_g and ΔA values for both damage states across DNS and ME. We notice that mismatch increases at lower frequencies, which is due to the manual calibration process favoring $\omega = 0.3\omega_0$. We believe this error to be surmountable with a more detailed parametric exploration, namely changing the quantities α and β in addition to the microscopic length parameter, to match the measured quantities across a wider frequency spectrum. Here, only the parameter l_m was used for calibration. From the analysis in Section 3, it is apparent that parameter combinations that match the apparent group velocity reduction are not unique. For instance, increasing the ratio α/β will also drop the group velocity (see Fig. 3 or Fig. 5) so that a different value of l_m could match the DNS values reported here. The unique identification of these parameters is a topic of future research. Of note is that the parameter δ, a measure of the microzone length relative to the input wavelength, is that as $\delta \to 1$ (a condition achieved by increasing the input signal frequency) the transmitted wave changes more dramatically in both shape and speed. Since $\alpha > \beta$ for these simulations, the group velocity reduction numerically observed is consistent with the analytical derivations in Section 3.

These results show the potential of ME to act as a physics-based measurement model to identify a particular damage state in solids within the context of NDE. Specifically, the pitch-catch scenario modeled herein, where one sensor sends a signal and another receives it, creates a situation where the time history of the receiving signal undergoes frequency-dependent changes in both shape and speed for different damage states. To understand this claim, consider using CE as a measurement model to detect damage. One may monitor CE modulus E and density ρ over time that match a particular pitch-catch transmission speed, but any one combination of CE parameters produces one frequency independent wave speed $\bar{c} = \sqrt{E/\rho}$. This means that the calibration of E and ρ from sent and received signals will change for different frequencies,

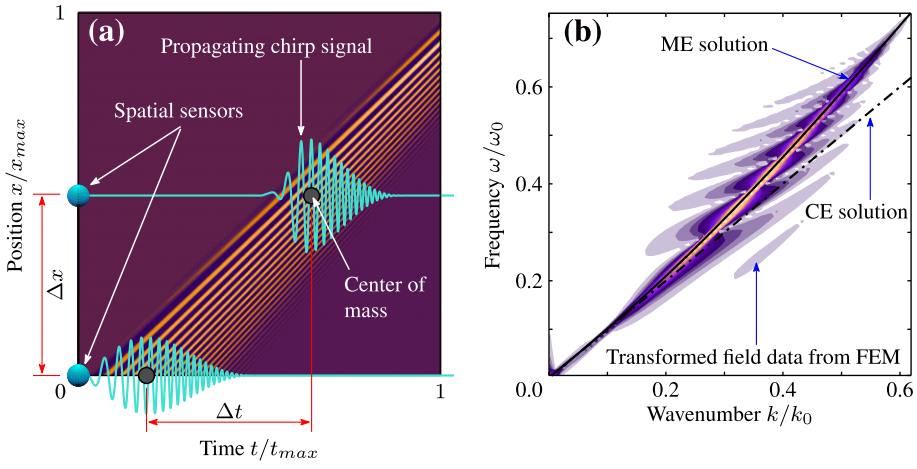

Fig. 7. Numerical data extraction methods in (a) space-time where spatial sensor locations are fixed and time histories superimposed on the wave field are measured and (b) wavenumber-frequency domains. The transformation from (a) to (b) is done with a DFT approach, and the finite element approximation in (b) is shown to match the analytical solution for the acoustic mode from Eq. (13). Parameters are $\alpha = 0.3$, $\beta = 0.9$, $\gamma = 0$, $\delta \approx 10$, $v_f = 0$, and $\psi = 1.0$ (undamaged).

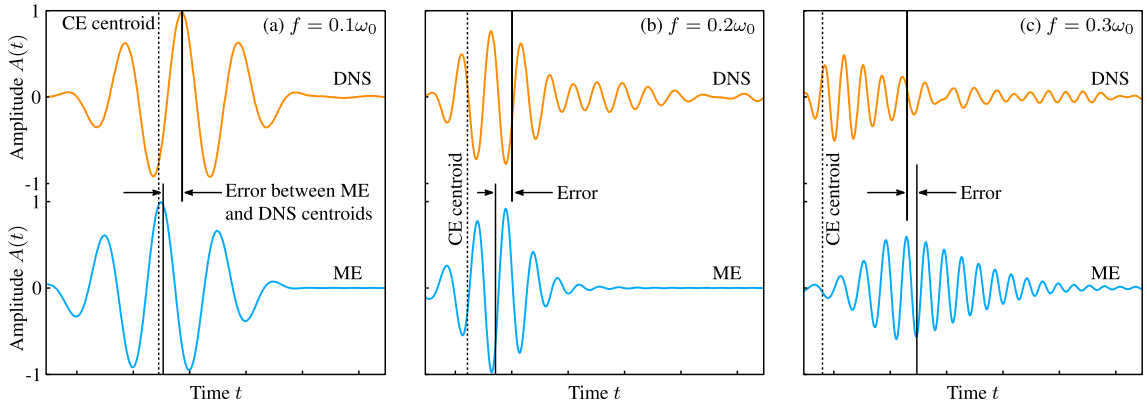

Fig. 8. Receiving sensor $s2$ time histories in Fig. 6 for DNS and ME for (a) $\omega = 0.1\omega_0$, (b) $\omega = 0.2\omega_0$, and (c) $\omega = 0.3\omega_0$. On each subfigure the time range is identical for DNS and ME simulations, and the CE wave signal centroids are shown with dotted lines. DNS and ME centroids are solid vertical lines. If ME predictions perfectly matched DNS damage state group velocities, the solid lines in each subfigure would overlap. Noticeable frequency-dependent lag between the undamaged, CE solution and both DNS and ME is observed.

Table 1
Comparison of DNS and ME simulations. For damage state 1, the DNS void size is $l_v = 100(\mu\text{m})$ and calibrated ME length parameter $l_m = 455(\mu\text{m})$. For damage state 2, $l_v = 200(\mu\text{m})$ and $l_m = 769(\mu\text{m})$. All table values are percent change relative to classical elasticity solution.

ω/ω_0	Damage state 1		Damage state 2	
	DNS	ME	DNS	ME
(a) Group velocity change $\Delta c_g(\%)$				
0.1	−4.9	−0.8	−9.9	−3.7
0.2	−9.0	−5.6	−22.6	−21.1
0.3	−15.8	−16.5	−36.4	−33.2
(b) Peak amplitude change $\Delta A(\%)$				
0.1	−2.1	−0.77	−8.4	−4.0
0.2	−22.5	−8.26	−46.1	−38.8
0.3	−49.3	−40.85	−77.4	−67.2

meaning that no one set of CE parameters could fit multiple input-output signal combinations even though the material remains unchanged in its current microstructure state and should thus have constant apparent stiffness and density. Furthermore, such a method provides little to no information about the length scale at which damage occurs or its effect on the macroscopic stiffness of the material.

Using ME, on the other hand, allows for one combination of material parameters to approximate a set of signals at different frequencies and is thus more consistent with reality in that boundary conditions should not affect material properties. As another nicety, the formulation includes a length parameter which gives insight onto the scale to which damage has grown over time. As shown in Table 1, the DNS voids of size l_v are roughly 1/4 the size of parameter l_m for damage states 1 and 2. This is physically consistent with the illustration in Fig. 1, as the parameter l_m is not meant to be the void size itself but the size of a mesoscopic averaging domain which contains statistical information about geometric variation and inhomogeneous deformation occurring in the microstructure. With that picture in mind, l_m is necessarily larger than one single inclusion or imperfection in the solid. The same concept was described by Gao et al. (1999) in their strain gradient plasticity formulation wherein one length parameter represents a domain that captures the interactions of dislocations within a meso-domain ensemble. Thus, the size of this averaging domain must increase as internal damage grows in size, since larger domains are required to contain the same amount of statistical information. For us, this means that as microstructural damage grows the microzone length parameter of ME ought to grow with it. The same would be true of stiff inclusions in a soft matrix, with the exception that $\beta > \alpha$ during the calibration process. In that case, the microstructure length parameter l_m would still grow in size as more microstructure is added as propagating wave would speed up with increasing inclusion volume fraction. These physical interpretations of ME are realized numerically in the results of this section.

As a final point to discuss, we previously remarked that backscattering was not captured with the computational ME simulations here. This limitation may be surmounted by giving the ME parameters $\{\alpha, \beta, \gamma, \delta\}$ a spatial distribution and fitting reflected signals in addition to transmitted ones. The discontinuity in material properties will create some backscattering, yet fitting reflected waveforms would be a far more complex problem than that studied here. Adding multiple response calibration would provide some uniqueness to the calibrated parameter values and include physically observed backscattering, two items absent from the elementary numerical examples presented here.

5. Conclusion

This study has presented a combination of analytical and computational results that elucidate the signatures of waves propagating in microelastic continua, continua described by additional degrees of freedom representing internal deformability of material particles. Analytical $\omega(k)$ dispersion relations were presented for the full 1D microelasticity model and extensive parametric studies were conducted on the results. These results showed that the ratio α/β of the high-order inertia to the high-order stiffness divides propagating wave velocities into positively and negatively dispersive regions with different high-frequency asymptotic behavior for each. The constitutive coupling parameter in the theory of elasticity with microstructure produces low frequency wave speeds that deviate from the classical elasticity solution. These conclusions demonstrate improved flexibility of microelasticity over gradient elasticity, which does not contain additional degrees of freedom, in predicting an array of wave speed signatures.

With an understanding of the dispersive properties of microelastic waves, we conducted numerical experiments to uncover the potential of computational microelasticity to identify damage states – a proxy for microstructure evolution – within heterogeneous solids. This was achieved by comparing time history data from virtual sensors in direct numerical simulation of a damaged material to those in an equivalent microelastic continuum.

Through these comparisons it was shown that by calibrating only the microelastic length parameter l_m, global trends of frequency-dependent and microstructure-dependent wave characteristics were captured through reductions of group velocity and maximum wave amplitude. Quantitatively, changes in group wave velocity more accurately matched DNS than the change in waveform shape. Matching both is a subject of future work and will require a more extensive parametric calibration procedure. The physical meaning of the length parameter in microelasticity is well suited to describe microstructure evolution in a solid as it was shown here that its calibrated values were consistent with the size of a statistical averaging domain consisting of an ensemble of voids.

Future work opportunities proliferate given the results of the current study. On the analytical side, tighter bounds should be derived for the model parameters based on propagation modes being confined to the real number line. Numerically, only 1D models were implemented, though there is a great opportunity for modeling more complex microstructures in multiple dimensions with computational microelasticity. In addition, more intelligent use of chirp signals and conversion of numerically generated microelastic wave fields to Fourier space is expected to yield more elegant damage identification algorithms that could become practical within NDE research. The dispersion relation of the optical mode representing the microstrain was reported, though a detailed numerical analysis of the microstrain fields was not. And finally, as microelasticity becomes better understood we expect to comparisons with physical experiments, not just direct numerical simulation of microstructures, to become more commonplace.

Acknowledgements

Steven Greene is supported by a National Science Foundation Graduate Research Fellowship and warmly thanks the NSF. Stefano Gonella thanks Bojan Guzina, Egor Dontsov and Roman Tokmashev of the University of Minnesota for the many discussions on the role of length scale parameters in gradient elasticity models. The Northwestern team also acknowledges NSF Grant CMMI-0823327.

References

Achenbach, J., 1973. Wave Propagation in Elastic Solids. North-Holland, New York.
Achenbach, J., 2000. Quantitative nondestructive evaluation. Int. J. Solids Struct. 37, 13–27.
Askes, H., Aifantis, E., 2009. Gradient elasticity and flexural wave dispersion in carbon nanotubes. Phys. Rev. B 80, 195412.
Askes, H., Metrikine, A., 2002. One-dimensional dynamically consistent gradient elasticity models derived from a discrete microstructure: Part2: Static and dynamic response. Eur. J. Mech. A-Solid. 21, 573–588.
Askes, H., Bennett, T., Aifantis, E., 2007. A new formulation and c0-implementation of dynamically consistent gradient elasticity. Int. J. Numer. Methods Eng. 72, 111–126.
Askes, H., Metrikine, A., Pichugin, A., Bennett, T., 2008a. Four simplified gradient elasticity models for the simulation of dispersive wave propagation. Philos. Mag. 88, 3415–3443.
Askes, H., Wang, B., Bennett, T., 2008b. Element size and time step selection procedures for the numerical analysis of elasticity with higher-order inertia. J. Sound Vib. 314, 650–656.
Belytschko, T., Liu, W., Moran, B., 2000. Nonlinear Finite Elements for Continua and Structures. Wiley, New York.
Bennett, T., Askes, H., 2009. Finite element modelling of wave dispersion with dynamically consistent gradient elasticity. Comput. Mech. 43, 815–825.
Chen, Y., Lee, J., 2003. Determining material constants in micromorphic theory through phonon dispersion relations. Int. J. Eng. Sci. 41, 871–886.
Droin, P., Berger, G., Laugier, P., 1998. Velocity dispersion of acoustic waves in cancellous bone. IEEE T. Ultrason. Ferr. 45, 581–592.
Eringen, A., 1999. Microcontinuum Field Theories I: Foundations and Solids. Springer-Verlag, New York.
Erofeyev, V.I., 2003. Wave processes in solids with microstructure. Stability, Vibration and Control of Systems. World Scientific, River Edge, NJ.
Gao, H., Huang, Y., Nix, W., Hutchinson, J., 1999. Mechanism-based strain gradient plasticity I. Theory. J. Mech. Phys. Solids 47, 1239–1263.
Germain, P., 1973. The method of virtual power in continuum mechanics. Part 2: Microstructure. SIAM J. Appl. Math. 25, 556–575.
Gonella, S., Ruzzene, M., 2008. Homogenization and equivalent in-plane properties of two-dimensional periodic lattices. Int. J. Solids Struct. 45, 2897–2915.
Gonella, S., Greene, M., Liu, W., 2011. Characterization of heterogeneous solids via wave methods in computational microelasticity. J. Mech. Phys. Solids 59, 959–974.
Lai, C., Rix, G., Foti, S., Roma, V., 2002. Simultaneous measurement and inversion of surface wave dispersion and attenuation curves. Soil Dyn. Earthquake Eng. 22, 923–930.
Ma, J., Maris, H., 2010. Localized vibrational modes in bars and plates. J. Appl. Phys. 107, 104904.
Metrikine, A., Askes, H., 2002. One-dimensional dynamically consistent gradient elasticity models derived from a discrete microstructure: Part 1: Generic formulation. Eur. J. Mech. A-Solid 21, 555–572.
Metrikine, A., Askes, H., 2006. An isotropic dynamically consistent gradient elasticity model derived from a 2d lattice. Philis. Mag. 86, 3259–3286.
Mindlin, R., 1964. Micro-structure in linear elasticity. Arch. Ration. Mech. An. 16, 51–78.
Murakami, H., Hegemier, G., 1986. Mixture model for unidirectionally fiber-reinforced composites. J. Appl. Mech. 53, 765–773.
Papacharalampopoulos, A., Vavva, M.G., Protopappas, V.C., Fotiadis, D., Polyzos, D., 2011. A numerical study on the propagation of rayleigh and guided waves in cortical bone according to mindlin's form ii gradient elastic theory. J. Acoust. Soc. Am. 130, 1060–1070.
Papargyri-Beskou, S., Polyzos, D., Besko, D., 2009. Wave dispersion in gradient elastic solids and structures: a unified treatment. Int. J. Solids Struct. 46, 2751–3759.
Philippidis, T., Aggelis, D., 2005. Experimental study of wave dispersion and attenuation in concrete. Ultrasonics 43, 584–595.
Polyzos, D., Fotiadis, D., 2012. Derivation of mindlins first and second strain gradient elastic theory via simple lattice and continuum models. Int. J. Solids Struct. 49, 470–480.
Polyzos, D., Tsepoura, K., Beskos, D., 2005. Transient dynamic analysis of 3-d gradient elastic solids by bem. Comput. Struct. 83, 783–792.
Song, F., Huang, G., Varadan, V., 2010. Study of wave propagation in nanowires with surface effects by using a high-order continuum theory. Acta Mech. 209, 129–139.
Stavropoulou, M., Exadaktylos, G., Papamichos, E., Larsen, I., Ringstad, C., 2003. Rayleigh wave propagation in intact and damaged geomaterials. Int. J. Rock Mech. Min. 40, 377–387.
Suiker, A., Metrikine, A., de Borst, R., 2001. Comparison of wave propagation characteristics of the cosserat continuum model and corresponding discrete lattice models. Int. J. Solids Struct. 38, 1563–1583.
Tauchert, T., Guzelsu, A., 1972. An experimental study of dispersion of stress waves in a fiber-reinforced composite. J. Appl. Mech. 39, 98–102.
Vavva, M.G., Protopappas, V.C., Gergidis, L.N., Charalambopoulos, A., Fotiadis, D., Polyzos, D., 2009. Velocity dispersion of guided waves propagating in a free gradient elastic plate: Application to cortical bone. J. Acoust. Soc. Am. 125, 3414–3427.
Vernerey, F., Liu, W., Moran, B., 2007. Multi-scale micromorphic theory for hierarchical materials. J. Mech. Phys. Solids 55, 2603–2651.
Wang, Q., 2005. Wave propagation in carbon nanotubes via nonlocal continuum mechanics. J. Appl. Phys. 98, 124301.
Yoon, J., Ru, C., Mioduchowski, A., 2003. Sound wave propagation in multiwall carbon nanotubes. J, Appl. Phys. 93, 4801–4806.
Yuan, S., Wang, L., Peng, G., 2005. Neural network method based on a new damage signature for structural health monitoring. Thin. Wall. Struct. 43, 553–563.
Zervos, A., 2008. Finite elements for elasticity with microstructure and gradient elasticity. Int. J. Numer. Methods Eng. 73, 564–595.